LA-UR-14-23072
Approved for public release; distribution is unlimited.

Title: Modeling the thermal deformation of TATB-based explosives. Part 1: Thermal expansion of “neat-pressed” polycrystalline TATB

Author(s): Luscher, Darby J.

Intended for: Report

Issued: 2014-05-08 (rev.1)

Modeling the thermal deformation of TATB-based explosives. Part 1: Thermal expansion of "neat-pressed" polycrystalline TATB

D.J. Luscher
Fluid Dynamics and Solid Mechanics Group, T-3
Los Alamos National Laboratory

April 29, 2014

Abstract

We detail a modeling approach to simulate the anisotropic thermal expansion of polycrystalline (1,3,5-triamino-2,4,6-trinitrobenzene) TATB-based explosives that utilizes microstructural information including porosity, crystal aspect ratio, and processing-induced texture. This report, the first in a series, focuses on nonlinear thermal expansion of "neat-pressed" polycrystalline TATB specimens which do not contain any binder; additional complexities related to polymeric binder and irreversible ratcheting behavior are briefly discussed, however detailed investigation of these aspects are deferred to subsequent reports.

In this work we have, for the first time, developed a mesoscale continuum model relating the thermal expansion of polycrystal TATB specimens to their microstructural characteristics. A self-consistent homogenization procedure is used to relate macroscopic thermoelastic response to the constitutive behavior of single-crystal TATB. The model includes a representation of grain aspect ratio, porosity, and crystallographic texture attributed to the consolidation process. A quantitative model is proposed to describe the evolution of preferred orientation of graphitic planes in TATB during consolidation and an algorithm constructed to develop a discrete representation of the associated orientation distribution function. Analytical and numerical solutions using this model are shown to produce textures consistent with previous measurements and characterization for isostatic and uniaxial "die-pressed" specimens.

Predicted thermal strain versus temperature for textured specimens are shown to be in agreement with corresponding experimental measurements. Using the developed modeling approach, several simulations have been run to investigate the influence of microstructure on macroscopic thermal expansion behavior. Results from these simulations are used to identify qualitative trends. Implications of the identified trends are discussed in the context of thermal deformation of engineered components whose consolidation process is generally more complex than isostatic or die-pressed specimens. Finally, an envisioned application of the modeling approach to simulating thermal expansion of weapon systems and components is outlined along with necessary future work to introduce the effects of binder and ratcheting behavior.

Key conclusions from this work include the following. Both porosity and grain aspect ratio have an influence on the thermal expansion of polycrystal TATB considering realistic material variability. The preferred orientation of the single crystal TATB [001] poles within a polycrystal gives rise to pronounced anisotropy of the macroscopic thermal expansion. The extent of this preferred orientation depends on the magnitude of deformation, and consequently, is expected to vary spatially throughout manufactured

components much like porosity. The modeling approach presented here has utility toward bringing spatially variable microstructural features into macroscale system engineering models.

1 Introduction

This report is the first in a series focused on continuum modeling of the thermal deformation of TATB-based explosives. These explosives are a composite material comprising a relatively high volume fraction (95% by weight) of the molecular crystal TATB (1,3,5-triamino-2,4,6-trinitrobenzene) while the balance is a polymeric binder whose function is to hold the explosive crystals together. This report focuses on the thermal expansion of "neat-pressed" polycrystalline TATB specimens that do not contain any binder. The thermal deformation of TATB-based explosives exhibits (1) non-linear thermal expansion that depends upon microstructure features which are significantly affected by details of the consolidation or manufacturing process and (2) a ratcheting behavior that manifests as irreversible deformation accumulating with temperature cycles. This work is focused solely on the influence of microstructure and material processing details on the nonlinear thermal expansion (i.e. 1) and defers details of ratcheting behavior (i.e. 2) to a subsequent investigation.

TATB is a relatively insensitive explosive molecular crystal used in several polymer bonded explosives including PBX-9502, LX-17, and ultrafine TATB (Maienschein and Garcia, 2002; Skidmore et al., 2003). Single crystal TATB possesses a triclinic unit cell and has strongly anisotropic elastic and thermal expansion properties (Kolb and Rizzo, 1979; Bedrov et al., 2009) . Understanding and modeling thermal expansion of polycrystalline TATB-based composites is an important aspect of thermomechanical models of high-explosives used for providing guidance to design and operational decisions especially regarding the safety and integrity of weapon system components. A detailed understanding of several aspects of the thermal expansion of TATB composites has eluded researchers for several decades (Skidmore et al., 2003; Souers et al., 2011). It is well known that the processing of explosives has a profound influence on the measured thermal expansion. It is also well known that dominant alignment of the basal plane in preferred orientations leads to pronounced anisotropy of the thermal expansion of TATB composites (Cady, 1975; Rizzo et al., 1981; Skidmore et al., 2003).

Kolb and Rizzo (1979) employed x-ray diffraction to measure lattice parameters of single crystal TATB over a range of temperatures and provided the first estimates of "bulk" thermal expansion for polycrystals. Importantly, they observed that thermal expansion and contraction of single crystal TATB is completely reversible and that the crystalline c-axis expands at a rate an order of magnitude more than for a- or b-axes. Rizzo et al. (1981) investigated thermal expansion and volumetric ratcheting for a variety of TATB-based polycrystal composites including neat-pressed TATB. They report linearized coefficients of thermal expansion along axial directions for cylindrical specimens and demonstrate that the TATB formulation and pressing condition influence thermal expansion rates, while characteristics of and amount of binder influence the ratcheting behavior. Skidmore et al. (2003) reviewed previous thermal expansion data and performed additional thermal expansion measurements on cylindrical specimens sampled at different orientations from a larger, "quasi-isostatically" pressed component. They relay the importance of pressing-induced texture to the observed anisotropy of thermal expansion in polycrystalline specimens. Cunningham et al. (2003) measured thermal expansion and ratchet growth during temperature cycles of pure TATB, LX-17 (92.5%

TATB, 7.5% kel-F binder), and PBX-9502 (95% TATB, 5% kel-F binder) and report axial and diametral strain across temperatures ranging from -60°C to 220°C. Their results indicate that die-pressed pure TATB polycrystal specimens exhibit axial rates of thermal expansion approximately twice that in the radial direction. Maienschein and Garcia (2002) presented similar work, but focused on the explosive LX-17 and did not include data for neat-pressed TATB polycrystal specimens. Souers et al. (2011) summarize results from several experiments on LX-17, PBX-9502, and ultrafine TATB, the latter being defined as having a significantly smaller characteristic particle size than normal TATB polycrystals.

There has been progress in modeling the thermal expansion behavior of TATB-based composites, most notably, Gee et al. (2007); Maiti et al. (2008) have developed a mesoscale model employing molecular dynamics to simulate irreversible thermal expansion of TATB-based explosives and the influence of binder strength and particle size distributions on ratcheting behavior. Such models help provide an understanding of the mechanisms involved during thermal deformation of TATB composites, but are not tractable for large-scale continuum constitutive description of material response that would be employed in, for example, a finite-element model of weapon system response to fluctuating environmental conditions.

Here, we report on detailed continuum modeling employing homogenization techniques to quantify, for the first time, the relationship between grain morphology (texture, porosity, and shape) and the composite thermal expansion behavior of pure TATB polycrystalline specimens. The models developed in this paper are a step towards a continuum thermomechanical constitutive description for the irreversible strain-ratcheting behavior demonstrated by TATB-based composites during cyclic temperature changes. However, the focus of this paper is not on the ratcheting mechanism itself, but instead on the effective reversible thermal expansion behavior of pure TATB composites (i.e. no binder) as a first critical step towards a general constitutive theory.

The balance of this report is organized as follows. Section 2 discusses thermoelastic properties of single-crystal TATB measured from atomistic simulation and experiments. Theoretical aspects of both the continuum homogenization and modeling the evolution of texture, as well as details of numerical implementation, are presented in Section 3. In Section 4 simulation results are compared with experimental measurements and used to establish credibility in trends identified between microstructure characteristics and macroscopic thermal expansion. Implications to the macroscale response of engineered components are presented in Section 5 along with an outline for applying the developed modeling approach to finite-element simulations of weapon system response. Finally a brief summary of the work, conclusions, and needed future work are highlighted in Section 6.

2 Thermoelasticity of single-crystal TATB

Variation of crystal lattice parameters due to temperature changes

The thermal expansion of single crystals of TATB has been experimentally measured using x-ray diffraction independently by Kolb and Rizzo (1979) and Sun et al. (2010), and numerically simulated using molecular dynamics (Gee et al., 2004; Taylor, 2013) and Monte Carlo techniques (Sewell, 1996; Rai et al., 2008), both employing empirical (or empirically fit) potential-based force fields. Experimental results of Kolb and Rizzo (1979) and Sun et al. (2010) differ substantially, especially concerning the thermal expansion rates. The

Table 1: Rates of thermal expansion in TATB lattice parameters from experimental and simulation data published in literature. Units are $\times 10^{-6}\, K^{-1}$.

Reference	$\bar{\alpha}_a$	$\bar{\alpha}_b$	$\bar{\alpha}_c$	Notes
Kolb and Rizzo (1979)	8.26	20.9	248	experiment
Sun et al. (2010)	11.3	10.4	167	experiment
Sewell (1996)	11	11	170	Monte Carlo
Gee et al. (2004)	24.6	24.9	134	molecular dynamics
Rai et al. (2008)	20	30	90	Monte Carlo
Taylor (2013)	15.8	16.8	57.6	molecular dynamics

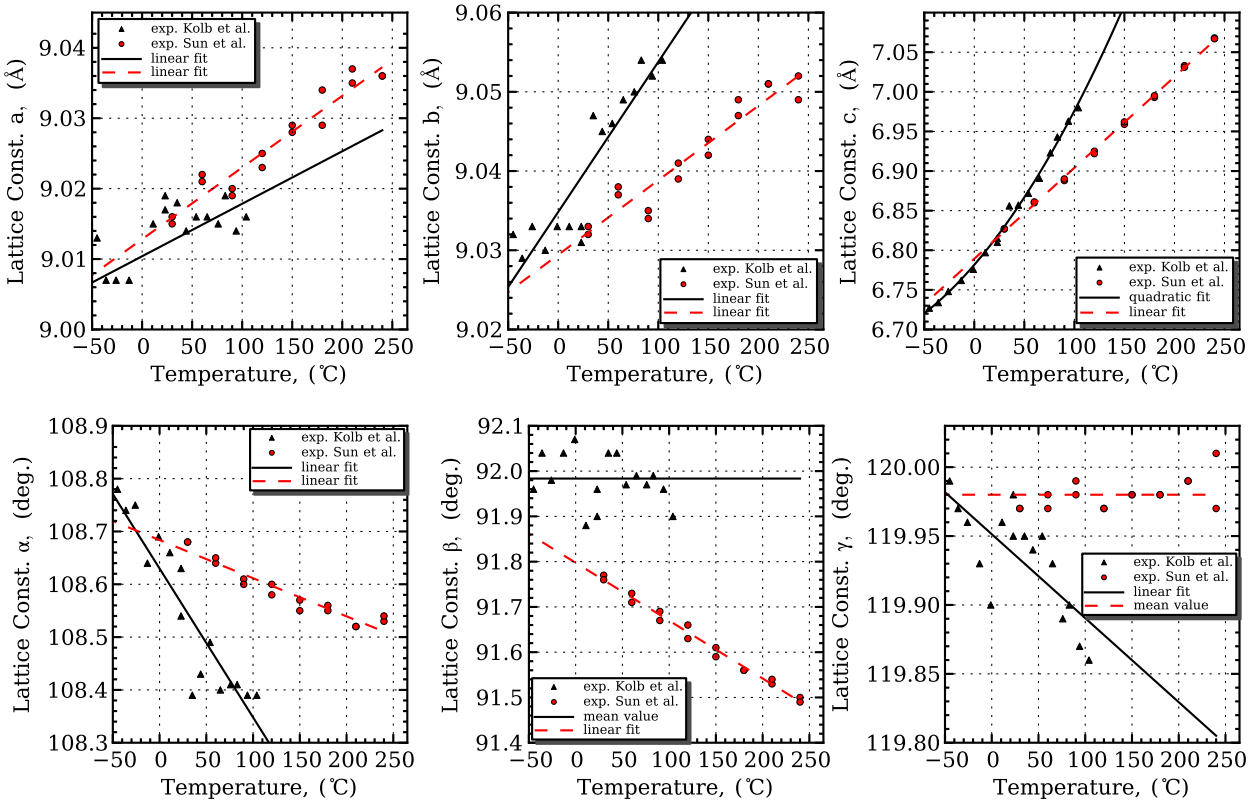

Figure 1: Variation of lattice parameters a, b, and c (top) and α, β, γ (bottom) with temperature and corresponding polynomial fits to data. Data from x-ray diffraction experiments Kolb and Rizzo (1979) and Sun et al. (2010).

works of Gee et al. (2004); Rai et al. (2008); Bedrov et al. (2009) and more recently Taylor (2013) reflect the state-of-the-art in simulating equilibrium crystal structure under various isothermal and isobaric conditions. Such techniques still struggle to capture rates of thermal expansion observed in experiment. For example, consider the linear rates of expansion computed by $\bar{\alpha} = \frac{1}{l}\frac{\partial l}{\partial T}$ for each cell length, a, b, and c, reported in Table 1. Clearly, there is not strong agreement across experiment and simulation techniques. Such properties are elusive because, for the case of simulation, they depend upon details of the interatomic potentials that are computationally intractable to include in a first-principles manner; consequently simplifying analytical assumptions made in developing appropriate potentials are significant to this behavior. Presumably, the experimental variation is attributed to specific processing dependent details leading to differences in crystal structure; for example, levels of impurities and initial specific mass densities are likely different across various laboratories (Zhang et al., 2012). Overall, comparing the results in Table 1 highlights that the thermal expansion of single-crystal TATB is not well characterized. It is of passing interest that more recent simulation results seem to be trending away from the predictions of lattice thermal expansion measured in either experiment.

Lattice parameters a, b, c, and α, β, γ measured by Kolb and Rizzo (1979) and independently by Sun et al. (2010) along with the corresponding best-fit polynomials are plotted in Fig. 1. The notable differences are (1) the expansion rate of the c-axis is much larger from measurements of Kolb and Rizzo (1979) than Sun et al. (2010); (2) variation of the length of c-axis appears to follow a quadratic behavior in measurements of Kolb and Rizzo (1979) leading to an increased rate of thermal expansion at higher temperatures; this behavior is not evident in the data of Sun et al. (2010); (3) expansion rates of a and b axes are similar in the Sun et al. (2010) measurements, but b expansion is more than double that of a in Kolb and Rizzo (1979); (4) the variation of β is more pronounced in results of Sun et al. (2010) than Kolb and Rizzo (1979); on the other hand, variations of α and γ are more pronounced in results of Kolb and Rizzo (1979) than Sun et al. (2010). It is possible that the differences in the processes used to synthesize TATB crystals by these two separate research groups result in different levels of, for example, impurities, which affect thermal expansion. Because the neat-pressed polycrystal TATB specimens used in the experiments we compare our model with use TATB crystals synthesized using the process listed in Kolb and Rizzo (1979) , the lattice thermal expansion measured by Kolb and Rizzo (1979) is used here.

Relationship between lattice parameter variations and continuum strain measures

In order to understand the importance of differences in lattice response within the context of continuum mesoscale behavior it is first necessary to relate variations in lattice parameters to continuum definitions of deformation, e.g., the second-order strain tensor. We outline the approach to convert measurements of evolving lattice parameters into continuum strain measures developed by Schlenker et al. (1978).

Associated with the triclinic Bravais lattice (cf. Fig. 2) is a natural triclinic (non-orthogonal) basis $\mathcal{B} = \{\mathbf{a}, \mathbf{b}, \mathbf{c}\}$, where the vectors $\mathbf{a}$, $\mathbf{b}$, and $\mathbf{c}$ are aligned with edges of the unit cell and whose magnitudes are the lattice parameters a, b, and c, respectively. We orient an orthonormal Cartesian crystal basis, $\mathcal{C} = \{\mathbf{e}_1^c, \mathbf{e}_2^c, \mathbf{e}_3^c\}$, such that $\mathbf{a} \cdot \mathbf{e}_1^c = a$, i.e., the 'x-direction' is aligned with the edge of the unit cell with lattice parameter a and $\mathbf{b} \cdot \mathbf{e}_3^c = 0$, i.e., the 'b-edge' lies in the 'xy-plane'. The transformation of tensor

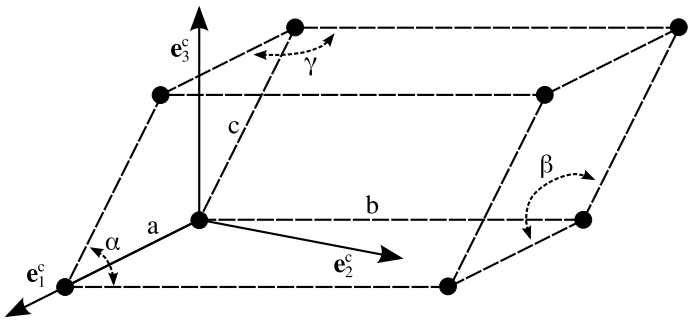

(a)

Figure 2: Geometric relationship between triclinic unit cell (with lattice parameters, a, b, c, α, β, γ) and the associated Cartesian crystal basis used here.

coefficients from basis $\mathcal{B}_i$ to $\mathcal{C}$ is computed as $\{\mathbf{v}\}_{\mathcal{C}} = [\mathbf{T}_i]\{\mathbf{v}\}_{\mathcal{B}_i}$, where

$$[\mathbf{T}_i] = \begin{bmatrix} a_i & b_i\cos\gamma_i & c_i\cos\beta_i \\ 0 & b_i\sin\gamma_i & d_i \\ 0 & 0 & e_i \end{bmatrix} \tag{1}$$

$d_i = c_i\left(\cos\alpha_i - \cos\gamma_i\cos\beta_i\right)/\sin\gamma_i$, $e_i = \left(c_i^2\sin^2\beta_i - d_i^2\right)^{1/2}$, and the subscript i denotes the i^{th} deformed state (Suh et al., 2000; He and Jonas, 2009). The notation $\{\mathbf{v}\}_{\mathcal{B}}$ is used to represent the array of coefficients of vector $\mathbf{v}$ resolved using the basis $\mathcal{B}$ and, likewise, $[\mathbf{A}]_{\mathcal{C}}^{\mathcal{B}}$ represents the matrix of coefficients of the second-order tensor, $\mathbf{A}$, against the mixed bases $\mathcal{B}$ and $\mathcal{C}$.

Accordingly, the coefficients of a position vector $\mathbf{X}$ can be expressed in either the triclinic lattice or Cartesian crystal bases and related to each other via $\{\mathbf{X}\}_{\mathcal{C}} = [\mathbf{T}_0]\{\mathbf{X}\}_{\mathcal{B}_0}$. Without a loss of generality, we can express the deformed position of a point in the unit cell with initial position $\mathbf{X}$ as $\mathbf{x} = \mathbf{F}\mathbf{X}$, where $\mathbf{F} = \frac{\partial \mathbf{x}}{\partial \mathbf{X}}$ is the deformation gradient within the unit cell. The coefficients of the deformed position vector are expressed in the Cartesian crystal basis as

$$\{\mathbf{x}\}_{\mathcal{C}} = [\mathbf{F}]_{\mathcal{C}}^{\mathcal{C}}\{\mathbf{X}\}_{\mathcal{C}} = [\mathbf{F}]_{\mathcal{C}}^{\mathcal{C}}[\mathbf{T}_0]\{\mathbf{X}\}_{\mathcal{B}_0} \tag{2}$$

At the same time, the transformation equation gives $\{\mathbf{x}\}_{\mathcal{C}} = [\mathbf{T}_i]\{\mathbf{x}\}_{\mathcal{B}_i}$ and when combined with Eq. 2 results in

$$\{\mathbf{x}\}_{\mathcal{B}_i} = [\mathbf{T}_i]^{-1}[\mathbf{F}]_{\mathcal{C}}^{\mathcal{C}}[\mathbf{T}_0]\{\mathbf{X}\}_{\mathcal{B}_0} \tag{3}$$

However, because vector coefficients reflecting the deformed position of a point fixed in the unit cell expressed in basis $\mathcal{B}_i$ are *identical* to the coefficients of the undeformed position of the same point expressed in the undeformed basis $\mathcal{B}_0$, Eq. 3 can be solved for

$$[\mathbf{F}_i]_{\mathcal{C}}^{\mathcal{C}} = [\mathbf{T}_i]\left[\mathbf{T}_0^{-1}\right] \tag{4}$$

Finally, applying Eqs. 1 and 4 to sets of lattice parameters characterizing the undeformed reference and deformed lattice configurations, i.e., $(a_0, b_0, c_0, \alpha_0, \beta_0, \gamma_0)$ and $(a_i, b_i, c_i, \alpha_i, \beta_i, \gamma_i)$, respectively, enables calculation of the components of the associated deformation gradient with respect to the Cartesian crystal basis,

$\mathcal{C}$. Using the deformation gradient associated with the deformed lattice, coefficients of the corresponding small strain tensor can be directly computed according to

$$\boldsymbol{\epsilon}_i = \mathrm{sym}\left[\mathbf{F}_i\right] - \mathbf{I} \tag{5}$$

The normal components of strain are thus evaluated as

$$\epsilon_{11} = \frac{a\left(T\right)}{a_\mathrm{r}} - 1 \tag{6a}$$

$$\epsilon_{22} = \frac{b\left(T\right)}{b_\mathrm{r}} \frac{\sin\gamma\left(T\right)}{\sin\gamma_\mathrm{r}} - 1 \tag{6b}$$

$$\epsilon_{33} = \frac{c\left(T\right)}{c_\mathrm{r}} \frac{e\left(T\right)}{e_\mathrm{r}} - 1 \tag{6c}$$

Expansion of the a, b, and c axes influences only the ϵ_{11}, ϵ_{22}, and, ϵ_{33} components of strain, respectively. Because of the alignment of our Cartesian frame with the a-axis of the triclinic lattice, the expression for ϵ_{11} is intuitive. Linear expansion of the a axis results in a linear coefficient of thermal expansion along ϵ_{11}, i.e., $\alpha_{11} = a'\left(T\right)/a_\mathrm{r}$ and does not depend on variations of any other lattice parameter. In general, linear thermal expansion of the b and c axes will not result in a linear thermal expansion expressed in the Cartesian basis if any of the lattice angles α, β, or γ vary with temperature. However, if the changes in angles are small, for example $\delta\gamma = \gamma - \gamma_\mathrm{r} << 1$, then $\sin\gamma \approx \sin\gamma_\mathrm{r} + \delta\gamma\cos\gamma_\mathrm{r}$ and, consequently, all normal components of thermal expansion can be approximated as linear with good agreement. Note, the accompanying linearized thermal expansion rates are influenced by even small variations of α, β, or γ. Of course, if the variation of c is nonlinear with respect to temperature, then ϵ_{33} will be nonlinear even for constant angles. Shear strains induced by stress-free thermal deformation involve variations of all unit cell lengths and angles and are not generally zero, i.e.,

$$\epsilon_{12} = \frac{a_\mathrm{r} b\left(T\right)\cos\gamma\left(T\right) - a\left(T\right) b_\mathrm{r}\cos\gamma_\mathrm{r}}{2a_\mathrm{r} b_\mathrm{r}\sin\gamma_\mathrm{r}} \tag{7a}$$

$$\epsilon_{23} = \frac{b_\mathrm{r} c\left(T\right) d\left(T\right)\sin\gamma_\mathrm{r} - b\left(T\right) c_\mathrm{r} d_\mathrm{r}\sin\gamma\left(T\right)}{2b_\mathrm{r} c_\mathrm{r} e_\mathrm{r}\sin\gamma_\mathrm{r}} \tag{7b}$$

$$\epsilon_{31} = \frac{a\left(T\right) b_\mathrm{r} c_\mathrm{r}\left(d_\mathrm{r}\cos\gamma_\mathrm{r} - \cos\beta_\mathrm{r}\sin\gamma_\mathrm{r}\right) - a_\mathrm{r} b\left(T\right) c_\mathrm{r} d_\mathrm{r}\cos\gamma\left(T\right) + a_\mathrm{r} b_\mathrm{r} c\left(T\right)\cos\beta\left(T\right)\sin\gamma_\mathrm{r}}{2a_\mathrm{r} b_\mathrm{r} c_\mathrm{r} e_\mathrm{r}\sin\gamma_\mathrm{r}} \tag{7c}$$

Strain components computed using Eq. 5 and the fits shown in Fig. 1 are plotted against temperature in Fig. 3. The apparent normal components of thermal expansion are linear over temperature with the exception of $\boldsymbol{\epsilon}_{33}$ (for the Kolb and Rizzo, 1979, data). As has been discussed previously by Kolb and Rizzo (1979) and subsequent works addressing thermal ratchet growth of TATB based explosives, the rate of thermal expansion in the Cartesian crystal $\mathbf{e}_3^c$ direction (aligned predominantly with the crystal c-axis) is an order of magnitude larger than that in the $\mathbf{e}_2^c$ direction which is approximately twice the value of that for the $\mathbf{e}_1^c$ direction. What has not been previously discussed is the shear coupling evident in Fig. 3. In particular, stress-free changes in temperature induce shear strain $\boldsymbol{\epsilon}_{23}$ at approximately the same rate as normal strain $\boldsymbol{\epsilon}_{22}$ which is a secondary effect considering the magnitudes of $\boldsymbol{\epsilon}_{11}$.

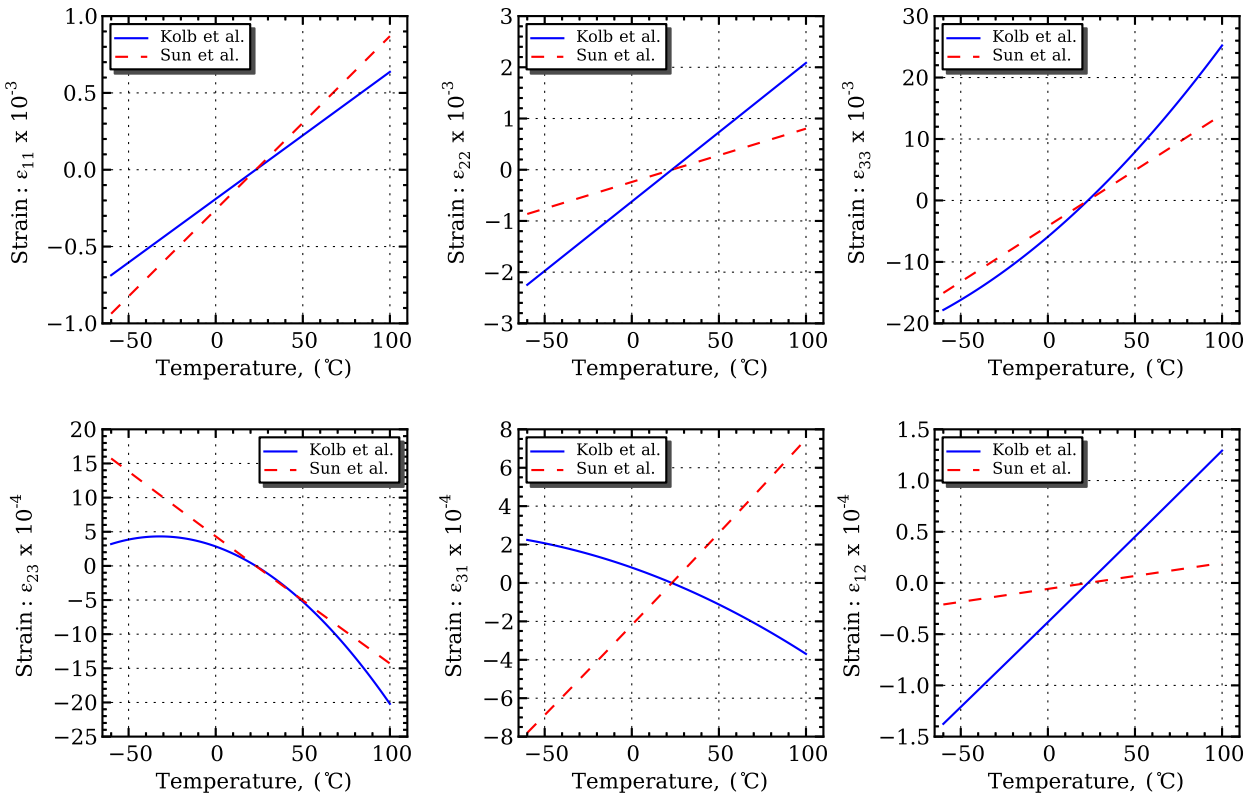

Figure 3: Components of thermal strain versus temperature from fits to experimental data of Kolb and Rizzo (1979); Sun et al. (2010).

Table 2: Anisotropic, tangent linear thermal expansion coefficients for TATB single crystals. All values are expressed with units of $10^{-6}\,^{\circ}\mathrm{C}^{-1}$

Source	α_{11}	α_{22}	α_{33}	α_{23}	α_{31}	α_{12}
Kolb (-30°C)	8.27	27.1	198	-0.6	-2.40	1.65
Kolb (23°C)	8.27	27.1	273	-15.6	-3.79	1.67
Kolb (55°C)	8.27	27.1	318	-24.5	-4.62	1.67
Sun (23°C)	11.3	10.4	181	-18.8	9.57	0.25

Table 3: TATB elastic stiffness coefficients as reported in Bedrov et al. (2009). All values are expressed using units of GPa.

Property	Value	Property	Value	Property	Value
L_{11}	65.7	L_{22}	62.0	L_{33}	18.3
L_{44}	1.4	L_{55}	0.68	L_{66}	21.6
L_{12}	18.5	L_{13}	4.0	L_{23}	5.0
L_{14}	-0.2	L_{15}	-1.0	L_{16}	1.0
L_{24}	0.6	L_{25}	-0.5	L_{26}	1.0
L_{34}	0.2	L_{35}	-0.4	L_{36}	-0.4
L_{45}	0.1	L_{46}	0.3	L_{56}	0.4

Elastic constants

Historically, it has not been possible to grow single crystals of TATB large enough to accommodate standard experimental approaches used for determining the full elasticity tensor. Consequently, elastic constants for single crystal TATB have not been measured experimentally. Only recently, calculations of elastic constants have been performed using molecular dynamics (Bedrov et al., 2009) and density functional theory (Valenzano et al., 2012). While there is some agreement between the parameters calculated by Bedrov et al. (2009) and those computed by Valenzano et al. (2012), the C_{11} coefficients differ by 19%; those predicted by Bedrov et al. (2009) are generally more compliant than those of Valenzano et al. (2012). Lattice parameters (i.e., a, b, c, α, β, γ) computed by Bedrov et al. (2009) are generally closer than those computed by Valenzano et al. (2012) to experimentally measured values Cady and Larson (1965) under ambient conditions. Additionally, the stiffnesses reported by (Valenzano et al., 2012) for another molecular crystal (PETN) are consistently stiffer than corresponding experimental measurements. We use the elastic constants computed by (Bedrov et al., 2009) as reported in Table 3. Incidentally, we have found only small differences in the computed macroscale thermal expansion using these different elastic moduli.

3 Theory

Heterogeneous Mesoscale

Consider a statistical volume element (SVE) of polycrystalline material at a scale of representation where heterogeneities exist due to varying orientation and shape of individual crystals interacting with porosity (voids). This mesoscale sits between that of a single-crystal (microscale) and the quasi-homogeneous macroscale. At any location, $\mathbf{x}$, within the mesoscale SVE the local relationship between stress and strain is given by thermoelastic constitutive relations, i.e.,

$$\boldsymbol{\epsilon}(\mathbf{x}) = \mathbb{M}(\mathbf{x}) : \boldsymbol{\sigma}(\mathbf{x}) + \boldsymbol{\epsilon}^{th}(\mathbf{x}, T) \tag{8}$$

where $\mathbf{x}$ denotes the position within the polycrystal, $\mathbb{M}$ is the spatially varying 4th order local compliance tensor and ϵ^{th} is a stress-free strain associated with thermal expansion under an evolving temperature, T.

Equivalently, the local fine scale response can be expressed as

$$\boldsymbol{\sigma} = \mathbb{L}\left(\mathbf{x}\right) : \left(\boldsymbol{\epsilon} - \boldsymbol{\epsilon}^{th}\left(\mathbf{x}, T\right)\right) \tag{9}$$

where $\mathbb{L} = \mathbb{M}^{-1}$ is the spatially varying local stiffness tensor. For polycrystal aggregates comprising various single crystals

$$\mathbb{M}\left(\mathbf{x}\right) = \left[\mathbf{Q} \boxtimes \mathbf{Q}\right] : \mathbb{M}^{c} : \left[\mathbf{Q} \boxtimes \mathbf{Q}\right]^{T} \qquad \text{and} \qquad \mathbb{L}\left(\mathbf{x}\right) = \left[\mathbf{Q} \boxtimes \mathbf{Q}\right] : \mathbb{L}^{c} : \left[\mathbf{Q} \boxtimes \mathbf{Q}\right]^{T} \tag{10}$$

where $\mathbf{M}^{c}_{ijkl}$ and $\mathbf{L}^{c}_{ijkl}$ are coefficients of the single-crystal compliance and stiffness tensors, respectively, resolved in the Cartesian crystal basis $\mathcal{C} = \{\mathbf{e}^{c}_{i}\}$, $\mathbf{Q}$ is a is a proper orthonormal rotation relating crystal base vectors to the SVE (or specimen) Cartesian base vectors $\mathbf{e}_i$ according to $\mathbf{e}^{c}_{i} = Q_{ij}\mathbf{e}_j$. Note, the '$\boxtimes$' operator is defined such that $\left[\mathbf{A} \boxtimes \mathbf{B}\right]_{ijkl} = A_{ik}B_{jl}$. In the case that all crystals have the same thermoelastic properties (with respect to the crystal basis), spatial heterogeneity in $\mathbb{M}\left(\mathbf{x}\right)$ arises due to the spatial distribution of crystal orientations, i.e., $\mathbf{Q}\left(\mathbf{x}\right) = \mathbf{Q}_{\alpha}\ \forall\, \mathbf{x} \in V_{\alpha}$ where V_{α} is the volume occupied by the α^{th} crystal.

Homogenized Macroscale

At the macroscale, for example within a weapon system finite element model, the relationship between mean-field stresses and strains is described by the homogenized constitutive behavior

$$\bar{\boldsymbol{\epsilon}} = \overline{\mathbb{M}} : \bar{\boldsymbol{\sigma}} + \bar{\boldsymbol{\epsilon}}^{th}\left(T\right) \tag{11}$$

or, equivalently,

$$\bar{\boldsymbol{\sigma}} = \overline{\mathbb{L}} : \left(\bar{\boldsymbol{\epsilon}} - \bar{\boldsymbol{\epsilon}}^{th}\left(T\right)\right) \tag{12}$$

The homogenization theories employed in this work to identify $\overline{\mathbb{L}} = \overline{\mathbb{M}}^{-1}$ and, more importantly, $\bar{\boldsymbol{\epsilon}}^{th}\left(T\right)$ from the heterogeneous mesoscale response are well-developed elsewhere (e.g. Kocks et al., 1998) and are explained only briefly here. Under quasistatic conditions, relations between the heterogeneous stress and strain fields within a polycrystal and the effective macroscale stress and strain are given by

$$\bar{\boldsymbol{\sigma}} = \frac{1}{V}\int_{V} \boldsymbol{\sigma}\left(\mathbf{x}\right) dV \tag{13}$$

and

$$\bar{\boldsymbol{\epsilon}} = \frac{1}{V}\int_{V} \boldsymbol{\epsilon}\left(\mathbf{x}\right) dV \tag{14}$$

respectively, where V is the volume of the SVE. Classical upper and lower bounds (concerning strain energy) associated with the homogenized coarse scale response are obtained through Voigt and Reuss assumptions of uniform strain and stress, respectively. Assuming uniform strain at the fine scale, i.e. $\boldsymbol{\epsilon}\left(\mathbf{x}\right) = \bar{\boldsymbol{\epsilon}}$, reduces the volume integral of Eq. 13 to the ensemble average

$$\bar{\boldsymbol{\sigma}} = \left\langle \mathbb{L}_{\alpha} : \left(\bar{\boldsymbol{\epsilon}} - \boldsymbol{\epsilon}^{th}_{\alpha}\right)\right\rangle \tag{15}$$

where the $\langle\cdot\rangle$ operator has been introduced to denote the ensemble average, $\sum_{\alpha}\frac{V_{\alpha}}{V}\left[\cdot\right]$. From Eq. 15 the following upper bound for homogenized constitutive behavior is directly obtained

$$\overline{\mathbb{L}}_{u} = \left\langle \mathbb{L}_{\alpha}\right\rangle \qquad\qquad \bar{\boldsymbol{\epsilon}}^{th}_{u} = \overline{\mathbb{L}}^{-1} : \left\langle \mathbb{L}_{\alpha} : \boldsymbol{\epsilon}^{th}_{\alpha}\right\rangle \tag{16}$$

In a similar fashion, the Reuss lower bound homogenized properties are computed assuming $\boldsymbol{\sigma}(\mathbf{x}) = \bar{\boldsymbol{\sigma}}$ resulting in

$$\overline{\mathbb{M}}_l = \langle \mathbb{M}_\alpha \rangle \qquad \bar{\boldsymbol{\epsilon}}_l^{th} = \left\langle \boldsymbol{\epsilon}_\alpha^{th} \right\rangle \tag{17}$$

The Hill estimate of these properties is computed by taking the average of upper and lower bounds, i.e.,

$$\overline{\mathbb{L}}_H = \frac{1}{2}\left[\overline{\mathbb{L}}_u + \overline{\mathbb{M}}_l^{-1}\right] \qquad \bar{\boldsymbol{\epsilon}}_H^{th} = \frac{1}{2}\left[\bar{\boldsymbol{\epsilon}}_l^{th} + \bar{\boldsymbol{\epsilon}}_u^{th}\right] \tag{18}$$

The main theoretical dilemma associated with these upper- and lower- bound homogenization schemes is that they are not physically consistent. For example, the uniform strain assumption is consistent with a compatible mesoscale displacement field, but the associated stresses evaluated from Eq. 9 do not generally satisfy equilibrium. On the other hand, an assumed uniform stress field does satisfy equilibrium, but the associated mesoscale strain field from Eq. 9 is generally incompatible.

Self-consistent homogenization schemes simultaneously satisfy compatibility requirements of the mesoscale displacement field, stress equilibrium, and the macro-homogeneity relation of Eqs. 13 and 14. Classically, Eshelby used Green's functions to solve for equilibrium stress and compatible strain fields for the case of an elastic inclusion embedded within a homogeneous matrix. In cases where the inclusion region can be described by an ellipsoidal geometry, the stress and strain fields are uniform within the inclusion (Eshelby, 1957). Eshelby's results were applied by Hill (1965) and Walpole (1969) to obtain a solution for stress and strain of elastic and elastoplastic single-crystals embedded within a homogenized matrix, and in turn, identify homogenization relationships. The theory was extended to develop a self-consistent theory of homogenization for thermoelastic-viscoplastic polycrystals (cf. Lebensohn et al., 2007) and to include effects of porosity (Lebensohn et al., 2004). We review the self-consistent homogenization theory employed in this work, briefly.

Eshelby's results relate the fluctuation stress field $\tilde{\boldsymbol{\sigma}} = \boldsymbol{\sigma} - \bar{\boldsymbol{\sigma}}$ to the fluctuation strain field $\tilde{\boldsymbol{\epsilon}} = \boldsymbol{\epsilon} - \bar{\boldsymbol{\epsilon}}$ by

$$\tilde{\boldsymbol{\epsilon}} = -\widetilde{\mathbb{M}} : \tilde{\boldsymbol{\sigma}} \tag{19}$$

where the interaction tensor $\widetilde{\mathbb{M}} = (\mathbb{I} - \mathbb{S})^{-1} : \mathbb{S} : \overline{\mathbb{M}}$, $\mathbb{I}$ is the 4th order identity tensor, and $\mathbb{S}$ is the Eshelby tensor which depends upon the shape of the embedded inhomogeneity and upon the macroscale compliance, $\overline{\mathbb{M}}$. From the local constitutive Eqs. 8, 9 and the interaction Eq. 19, the stress localization equation is obtained

$$\boldsymbol{\sigma}_\alpha = \mathbb{B}_\alpha : \bar{\boldsymbol{\sigma}} + \mathbf{b}_\alpha \tag{20}$$

where

$$\mathbb{B}_\alpha = \left(\mathbb{M}_\alpha + \widetilde{\mathbb{M}}\right)^{-1} : \left(\mathbb{M} - \widetilde{\mathbb{M}}\right) \tag{21}$$

and

$$\mathbf{b}_\alpha = \left(\mathbb{M}_\alpha + \widetilde{\mathbb{M}}\right)^{-1} : \left(\bar{\boldsymbol{\epsilon}}^{th}(T) - \boldsymbol{\epsilon}_\alpha^{th}(T)\right) \tag{22}$$

Note, $\mathbf{b}_\alpha$ is the contribution to the local mesoscale stress in the α^{th} crystal attributed to the difference between the stress-free crystal and macroscale polycrystal thermal expansion. Substitution of the stress

localization equation or, equivalently, a strain localization equation into the macro-homogeneity relation $\bar{\boldsymbol{\sigma}} = \langle \boldsymbol{\sigma} \rangle$ or $\bar{\boldsymbol{\epsilon}} = \langle \boldsymbol{\epsilon} \rangle$, respectively, provides the self-consistent homogenization relations

$$\overline{\mathbb{M}} = \langle \mathbb{M}_\alpha : \mathbb{B}_\alpha \rangle : \langle \mathbb{B}_\alpha \rangle^{-1} \tag{23}$$

and

$$\bar{\boldsymbol{\epsilon}}^{th}(T) = \left\langle \mathbb{M}_\alpha : \mathbf{b}_\alpha + \boldsymbol{\epsilon}_\alpha^{th}(T) \right\rangle - \overline{\mathbb{M}} : \langle \mathbf{b}_\alpha \rangle \tag{24}$$

Equations 23 and 24 are implicit nonlinear equations solved in this work using a general nonlinear solver built into Scipy, an open-source scientific numerical computation module for Python. The compliance of a void inclusion is infinite and, consequently, Eqs. 21 and 22 cannot be evaluated directly for the pore phase. Lebensohn et al. (2004) demonstrate that Eq. 23 can be computed using the relationships $\mathbb{M}_{\mathrm{v}} : \mathbb{B}_{\mathrm{v}} = \mathbb{A}_{\mathrm{v}} : \mathbb{M}$ and $\mathbb{B}_{\mathrm{v}} = 0$, where

$$\mathbb{A}_{\mathrm{v}} = \left(\widetilde{\mathbb{M}} : \mathbb{L} + \mathbb{I} \right) \tag{25}$$

and the subscript 'v' denotes void phase. Likewise, Eq. 24 is evaluated using the relationships $\mathbb{M}_{\mathrm{v}} : \mathbf{b}_{\mathrm{v}} + \boldsymbol{\epsilon}_{\mathrm{v}}^{th}(T) = \mathbb{A}_{\mathrm{v}} : \overline{\boldsymbol{\epsilon}}^{th} + \mathbf{a}_{\mathrm{v}}$ and $\mathbf{b}_{\mathrm{v}} = \mathbf{0}$, where

$$\mathbf{a}_{\mathrm{v}} = -\widetilde{\mathbb{L}}^{-1} : \mathbb{L} : \overline{\boldsymbol{\epsilon}}^{th} \tag{26}$$

Modeling the initial textured state from consolidation

Application of homogenization approaches depend upon a discrete representation, i.e. $\{\mathbf{Q}_i \; \forall \, i \in [1..N]\}$, of the orientation distribution function (ODF) for the grains in the polycrystal. For cases where there is no dominant or 'preferred' orientation of crystals in the polycrystalline material, the ODF reflects a uniform distribution of all orientations. If there is one or more preferred orientations, or, more generally, a nonuniform ODF, the aggregate is textured and the homogenized properties will exhibit anisotropy.

There are three main processing conditions associated with explosives: (1) isostatic pressing, (2) and uniaxial (die) pressing, and (3) quasi-isostatic pressing, . Under cases of isostatic pressing (1), the consolidation process is nearly volumetric, i.e., there is no distortion of the original pressing shape, and the resulting component exhibits essentially no texture. On the other hand, uniaxial pressing (2) tends to realign the [001] poles toward the axis of consolidation (Rizzo et al., 1981; Cady, 1975; Skidmore et al., 2003). This process is often employed for pressing of cylindrical test specimens with application to, e.g., thermal expansion and ratchet growth experiments. The consolidation process used to manufacture weapon system components are somewhere in between isostatic and uniaxial pressings; thus, such processes are referred to loosely as quasi-isostatic and it is expected that the resulting components exhibit a spatially variable texture.

There is a significant amount of thermal expansion and ratchet growth data in the literature associated with various pressing conditions, but very few measurements of the actual texture associated with the test specimens. Simulating the effects of these differing processing conditions on thermal expansion behavior requires first predicting the textured state of the material. Here a proposed texture evolution model is used to explore the influence of processing on macroscale material properties; in the future, such models can be used to understand effects of more general processing conditions.

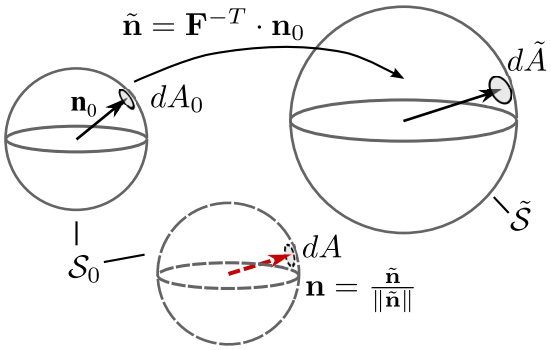

Figure 4: Illustration of the mapping of pole orientations and associated spheres.

Previous work by Schwarz et al. (2013) to model the texture evolution of the high explosive PBX-9502 adopted the phenomenology that the preferred orientation of TATB crystals is aligned in the direction of maximum shearing strain associated with the consolidation process. Their conceptual model is consistent with the idea that, during consolidation, the deformation is accommodated by shear-driven slip along graphitic planes of the material. There are a few limitations of their model; most importantly for our application, it is of limited utility in continuum modeling because it does not give a quantitative distribution of crystal orientation, rather one single preferred orientation of [001] poles. Additionally, the implementation of their approach utilizes a subset of a symmetric two-dimensional plane strain tensor; thus, the preferred orientation is independent of the skew part of the displacement gradient. In other words, their model is not affected by material rotation. Finally, the phenomenology of their model aligns [001] poles normal to the orientation of maximum shear. Consequently, in a uniaxial (die) pressed specimen the Schwarz model predicts an axisymmetric ring of preferred orientation inclined 45° from the axis of pressing. This is inconsistent with experimental observations that the preferred orientation of [001] poles resulting from uniaxial consolidation is aligned with the pressing direction (Cady, 1975; Skidmore et al., 2003).

March (1932) developed a model for the orientation distribution of aggregates of "platy" crystals that have undergone deformation. The phenomenology of the model is purely geometric. The March model assumes that, because of the pronounced aspect ratio of "sheet-like" or "platy" crystals, the basal planes oriented normal to the thickness direction of each crystal convect with the deformation (Owens, 1973). Application of the March theory to cases of volume-preserving deformation along a primary axis results in the March-Dollase (Owens, 1973; Dollase, 1986) orientation distribution and has seen extensive use for experimental characterization of a variety of materials (cf. Owens, 1973; Baker et al., 1993; Zolotoyabko, 2013). Here we apply the March theory to cases of (1) isostatic and (2) uniaxial pressing to establish analytical expressions for the relative distribution of [001] poles in polycrystal TATB. Subsequently, we outline an approach to apply the March theory to modeling the evolution of the orientation of discrete polycrystal samples under arbitrary deformation.

A vector normal to a plane described by the collection of $\alpha = 1..N$ *material* lines, $\mathbf{l}_0^\alpha$, within the plane satisfies $\mathbf{n}_0 \cdot \mathbf{l}_0^\alpha = 0$. If the collection of *material* lines are mapped into a different configuration by an affine transformation $\mathbf{l}^\alpha = \mathbf{M}\mathbf{l}_0^\alpha$, then the normal to this plane in the new configuration is $\tilde{\mathbf{n}} = \mathbf{M}^{-T}\mathbf{n}_0$ such that the convected plane normal satisfies $\tilde{\mathbf{n}} \cdot \mathbf{l}^\alpha = 0$. This transformation represents the standard push-forward operation for a *covector*. A crystallographic pole represents the normal to a plane, and, as the spatial

gradient of a surface, transforms as a covector. Accordingly, the March model assumes that the poles normal to "sheet-like" crystalline planes transform with the deformation of the material during consolidation by

$$\tilde{\mathbf{n}} = \mathbf{F}^{-T}\mathbf{n}_0 \tag{27}$$

where $\mathbf{n}_0$ is a unit vector normal (to the $a-b$ plane in the triclinic lattice) in the reference configuration, $\tilde{\mathbf{n}}$ is the (non-unit) normal to the same plane in the current configuration and $\mathbf{F}$ is the deformation gradient mapping material vectors from the reference to current configurations. Figure 4 illustrates this mapping. Let the unit sphere, $\mathcal{S}_0$, of Figure 4 represent the orientation space of unit normal (pole) covectors, $\mathbf{n}_0$. We parameterize this orientation space by the angles θ_0 and ϕ_0 such that $\mathbf{n}_0 = \sin\theta_0\cos\phi_0\,\mathbf{e}_1 + \sin\theta_0\sin\phi_0\,\mathbf{e}_2 + \cos\theta_0\,\mathbf{e}_3$.

It is useful to note that the ratio between a region dA on the surface of a sphere and the total surface area, A, is equal to the ratio between the volume of the conical region (bounded by dA on the surface) and the total sphere volume, i.e.,

$$\frac{dA}{A} = \frac{dV}{V} \tag{28}$$

Furthermore, for a unit sphere ($A_0 = 4\pi$ and $V_0 = \frac{4}{3}\pi$), $dV_0 = 3\,dA_0$.

Consider an infinitesimal area, dA_0 surrounding the intersection of the vector $\mathbf{n}_0$ with the unit sphere $\mathcal{S}_0$ in Figure 4. In this manner dA_0 represents an infinitesimal region of orientation space. The number of poles whose orientation are contained within the orientation space dA_0 is $N = P(\theta_0,\phi_0)\,dA_0$, where $P(\theta_0,\phi_0)$ is a probability density. Equivalently, the probability distribution can be normalized by a constant coefficient to obtain a distribution of "multiples of a random uniform distribution", i.e.,

$$M_0(\theta_0,\phi_0) = cP(\theta_0,\phi_0) = cN/dA_0 \tag{29}$$

In this way, $M_0(\theta_0,\phi_0) = 1$ implies the orientation θ_0,ϕ_0 has the same relative occurrence as for a non-textured polycrystal.

The material is deformed from the reference configuration into the current configuration by the deformation gradient, $\mathbf{F}$, such that each of the poles that originally had the orientation $\mathbf{n}_0$ are now aligned with $\tilde{\mathbf{n}} = \mathbf{F}^{-T}\mathbf{n}_0$. Associated with this convected covector $\tilde{\mathbf{n}}$ is a sphere $\tilde{\mathcal{S}}$ whose radius reflects the "stretch" of a covector initially aligned with $\mathbf{n}_0$, i.e.,

$$R^2 = \frac{\tilde{\mathbf{n}}\cdot\tilde{\mathbf{n}}}{\mathbf{n}_0\cdot\mathbf{n}_0} = \mathbf{n}_0\cdot\left(\mathbf{F}^{-1}\mathbf{F}^{-T}\right)\cdot\mathbf{n}_0 = \left[\mathbf{n}\cdot\left(\mathbf{F}\mathbf{F}^{T}\right)\cdot\mathbf{n}\right]^{-1} \tag{30}$$

where the *unit* normal $\mathbf{n} = \tilde{\mathbf{n}}/\|\tilde{\mathbf{n}}\|$. The latter of Eq. 30, where $\mathbf{n} = \sin\theta\cos\phi\,\mathbf{e}_1 + \sin\theta\sin\phi\,\mathbf{e}_2 + \cos\theta\,\mathbf{e}_3$, provides a more convenient parameterization $R(\theta,\phi)$ rather than $R(\theta_0,\phi_0)$ provided by the second to last expression. The volume of $\tilde{\mathcal{S}}$ is

$$\tilde{V} = \frac{4}{3}\pi R^3 \tag{31}$$

and the infinitesimal volume within $\tilde{\mathcal{S}}$ that contains the N poles originally associated with orientation $\mathbf{n}_0$ is

$$d\tilde{V} = \det\mathbf{F}^{-1}dV_0 \tag{32}$$

The number of poles, N, contained within this region is unaffected by the deformation, but the area over which they intersect a unit sphere has changed, thus the orientation distribution is affected by the deformation. Specifically, N poles intersect the *unit* sphere $\mathcal{S}_0$ over a region $dA \neq dA_0$. Note that, because $\tilde{\mathbf{n}}$

is not a unit vector, $\tilde{\mathcal{S}}$ is not a unit sphere and accordingly, $d\tilde{A}$ is not the appropriate area for computing distribution of pole density. The intersection of the deformed volume $d\tilde{V}$ with the unit sphere $\mathcal{S}_0$ defines a deformed region of parameter space, dA, whose relationship with $\tilde{\mathcal{S}}$ is given by

$$\frac{dA}{A} = \frac{d\tilde{A}}{\tilde{A}} = \frac{d\tilde{V}}{\tilde{V}} \tag{33}$$

consequently, $dA = A\frac{d\tilde{V}}{\tilde{V}}$.

The relative orientation distribution is calculated by $M(\theta,\phi) = cN/dA$, and from Eq 29 above giving $M(\theta,\phi) = \frac{dA_0}{dA} M_0(\theta_0,\phi_0)$. Finally, from Eqs. 31-33 and the relationship $dV_0 = 3\, dA_0$ for a unit sphere,

$$M(\theta,\phi) = M_0(\theta_0,\phi_0) \det \mathbf{F}\; R(\theta,\phi)^3 \tag{34}$$

Below, it is shown that application of Equation 34 to the case of uniaxially die-pressed specimens results in an axisymmetric distribution of the alignment of [001] poles with the most likely alignment along the direction of pressing, i.e. $\theta = 0$, and smoothly decreasing to a minimum likelihood of alignment orthogonal to the pressing direction, i.e. $\theta = \frac{1}{2}\pi$. This expression is entirely consistent with experimental observations. It is not directly clear from Equation 34 that this model for texture evolution depends upon material rotation. To illustrate this aspect, we consider the case of a pure rotation. In this case, $\det \mathbf{F} = 1$ and $R(\theta,\phi)^3 = 1$. If the initial orientation distribution is uniform $M_0(\theta_0,\phi_0) = 1$ then there is no evolution of texture $M(\theta,\phi) = 1$, i.e., the rigid rotation of a uniform orientation distribution results in the same uniform distribution. On the other hand, if a specimen with an initial distribution $M_0(\theta_0,\phi_0) \neq 1$ undergoes a rigid rotation, then the resulting orientation distribution is $M(\theta,\phi) = M_0(\theta_0,\phi_0)$. This relationship correctly states that the likelihood of a crystal having its [001] in an orientation (θ,ϕ) after the rigid rotation is identical to the likelihood that a crystal initially had the [001] in an orientation (θ_0,ϕ_0). The relationship between initial and final orientations is known and provides the rotational relationship between the initial and final pole figure with respect to a fixed coordinate basis. Ignoring locations at which the following expressions possess singularities (which are mitigated by more detailed expressions), the initial orientations can be expressed as nonlinear functions of the final orientations, i.e.,

$$\phi_0 = \hat{\phi}_0(\theta,\phi) = \arccos\left[R_{13}\sin\theta\cos\phi + R_{23}\sin\theta\sin\phi + R_{33}\cos\phi\right] \tag{35}$$

$$\theta_0 = \hat{\theta}_0(\theta,\phi) = \arcsin\left[\frac{R_{11}\sin\theta\cos\phi + R_{21}\sin\theta\sin\phi + R_{31}\cos\phi}{R_{13}\sin\theta\cos\phi + R_{23}\sin\theta\sin\phi + R_{33}\cos\phi}\right] \tag{36}$$

where R_{ij} are coefficients of the rotation tensor $\mathbf{R}$ expressed in the fixed Cartesian basis. Along with Eqs. 35 and 36, for cases of pure material rotation,

$$M(\theta,\phi) = M_0\left(\hat{\theta}_0(\theta,\phi), \hat{\phi}_0(\theta,\phi)\right) \tag{37}$$

illustrates the dependence of the texture evolution model on material rotations. For general cases of deformation, both strain and rotation affect the final texture.

Application of Eq. 34 to the separate cases of isostatic and uniaxial pressing of an intially texture-free (i.e., $M_0(\theta_0,\phi_0) = 1$) specimen of polycrystalline TATB provides a qualitative validation of the phenomenology of the March theory. First consider the case of isostatic pressing. In this case, the deformation gradient is $\lambda\mathbf{I}$, where λ is the principal stretch of covectors (all three are equal) and is related to the volumetric deformation, i.e., $\det \mathbf{F} = \lambda^3$. Accordingly, $\tilde{\mathbf{n}} = \lambda^{-1}\mathbf{n}$, $R^3 = \lambda^{-3}$, which, upon substitution into Eq.

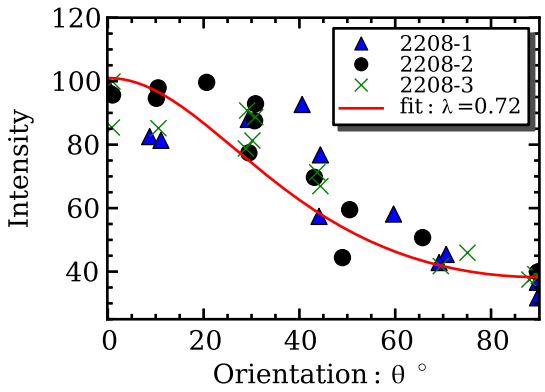

Figure 5: Comparison of distribution of [001] poles in unaxially pressed specimens as measured by Cady (1975) with fits of the analytical March distribution.

34, yields $M(\theta, \phi) = 1$. In other words, no texture results from a purely isostatic (or, more accurately, volumetric) consolidation process.

Assuming an initially uniform orientation distribution, i.e., $M_0(\theta_0, \phi_0) = 1$ and uniaxial deformation of a specimen from an initial thickness d_0 to a final thickness d such that

$$[\mathbf{F}] = \begin{bmatrix} 1 & 0 & 0 \\ 0 & 1 & 0 \\ 0 & 0 & d/d_0 \end{bmatrix} \tag{38}$$

leads to

$$M(\theta, \phi) = \frac{d}{d_0}\left[\sin^2\theta + \left(\frac{d}{d_0}\right)^2 \cos^2\theta\right]^{-\frac{3}{2}} \tag{39}$$

Cady used X-ray diffraction to measure the texture of uniaxially (die) pressed cylindrical specimens of TATB (Cady, 1975; Skidmore et al., 2003). The results were reported as plots of the "relative number of aligned crystals" versus the angle between the [001] pole and the specimen face. Using the relationship $\frac{I(\theta)}{I(\theta_r)} = \frac{M(\theta)}{M(\theta_r)}$, where $I(\theta)$ is the "relative number of aligned crystals" as reported by Cady, we fit the March equation to these measurements. Specifically, the relative pole figure intensity at an angle $\theta = 90°$ between the compression axis and [001] pole was estimated by averaging $I(90)$ for all specimens and symmetric measurements. The optimal value of the principal stretch, $\lambda = \frac{d}{d_0}$, that provided the least-square residual for the expression

$$\frac{I(\theta)}{I_{90°}} = \left[\sin^2\theta + \left(\frac{d}{d_0}\right)^2 \cos^2\theta\right]^{-\frac{3}{2}} \tag{40}$$

was identified as $\frac{d}{d_0} = 0.72$. The experimental data points and best-fit March distribution are plotted in Figure 5.

The March model for texture evolution in composites of platy crystals leads to the analytical expression of Eq. 39. However, application of the self-consistent approach to compute homogenized thermal expansion response requires a discrete representation (i.e. $\{\mathbf{Q}_i \; \forall \, i \in [1..N]\}$) of a full orientation distribution. For

example, a discrete set of grain volume fractions and their associated Euler angles defining the relationship between crystal and specimen bases.

One approach to generate such a sample is to begin with a discrete representation of uniform distribution and then apply the deformation of Eq 27 to each of the crystal poles and compute the resulting discrete sample of Euler angles. The algorithm begins with a set of N distinct orientations and corresponding volume fractions,

$$\mathcal{O}_0 = \{(\mathbf{Q}_0^\alpha, \mathrm{V}_\alpha)\, \forall \alpha \in [1..N]\} \tag{41}$$

that represent a uniform distribution of crystal orientations. In particular, we use the HEALPix algorithm developed by Gorski et al. (2005) to generate $\mathcal{O}_0$. The HEALPix algorithm constructs a uniform equal volume grid on the space of 3D orientations ($SO(3)$). For each of the crystals, coefficients of the [001] unit pole vector with respect to the specimen coordinate basis, $\mathbf{e}_i$ prior to deformation are computed as

$$\{\mathbf{n}_0^\alpha\}_i = [\mathbf{Q}_0^\alpha]_{i3} \tag{42}$$

The deformed pole vector for the α^{th} volume fraction is then computed according to

$$\tilde{\mathbf{n}}^\alpha = \mathbf{F}^{-T}\mathbf{n}_0^\alpha \tag{43}$$

and then normalized to a unit vector, i.e.,

$$\mathbf{n}^\alpha = \frac{\tilde{\mathbf{n}}^\alpha}{\|\tilde{\mathbf{n}}^\alpha\|} \tag{44}$$

The axis of a rotation that brings $\mathbf{n}_0^\alpha$ into alignment with $\mathbf{n}^\alpha$ is identified from the cross product of the two unit vectors, i.e.,

$$\mathbf{q}^\alpha = \frac{\mathbf{n}_0^\alpha \times \mathbf{n}^\alpha}{\|\mathbf{n}_0^\alpha \times \mathbf{n}^\alpha\|} \tag{45}$$

Likewise, the angle between $\mathbf{n}_0^\alpha$ and $\mathbf{n}^\alpha$ is computed as

$$\theta^\alpha = \arcsin\left[\mathbf{n}_0^\alpha \cdot \mathbf{n}^\alpha\right] \tag{46}$$

The orthonormal rotation that will bring the crystal basis $\mathbf{e}_i^c$ into alignment with the specimen basis $\mathbf{e}_i$ given the transformation of the lattice reflected by deformation of the [001] poles is computed using the exponential map and angle-axis rotation convention (Bauchau and Trainelli, 2003), i.e.,

$$\mathbf{Q}^\alpha = \exp\left[\widehat{\theta^\alpha \mathbf{q}^\alpha}\right] \cdot \mathbf{Q}_0^\alpha \tag{47}$$

where the operator $\widehat{\mathbf{v}}$ returns the skew tensor for which $\mathbf{v}$ is the axial vector. Computations of Eqs. 41-47 are repeated for each of the volume fraction of crystals in order to generate the textured orientation distribution $\mathcal{O}(\mathbf{F}) = \{(\mathbf{Q}^\alpha, \mathrm{V}_\alpha)\, \forall \alpha \in [1..N]\}$.

An alternate approach to simulating the evolution of texture for a discrete sampling of polycrystal orientations is to randomly sample Eq. 39 to build statistical realizations of discrete orientations drawn from the underlying analytical distribution function. Toth and van Houtte (1992) developed a method to construct a discrete set of grain orientations from a discrete representation of the cumulative distribution computed by integrating the underlying ODF over a uniform grid in orientation space. Each region within

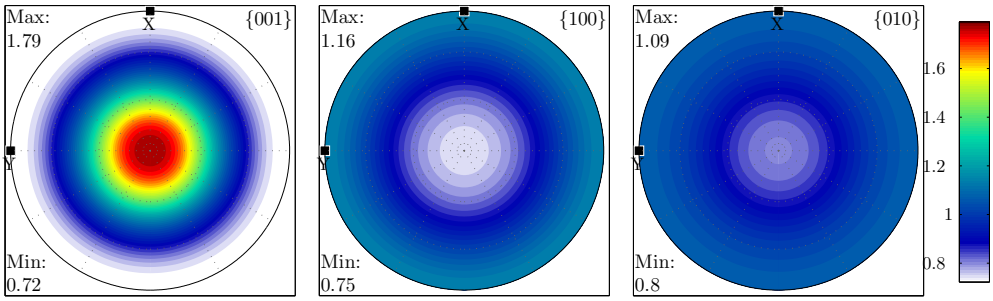

Figure 6: Pole figures from the simulated texture evolution of a discrete ($N = 4800$) orientation distribution representing the specimens examined by Cady. The [001] pole figure from the simulated discrete texture representation is consistent with the analytical March distribution of Eq. 39 for a uniaxial state of deformation along the specimen 'Z'-axis.

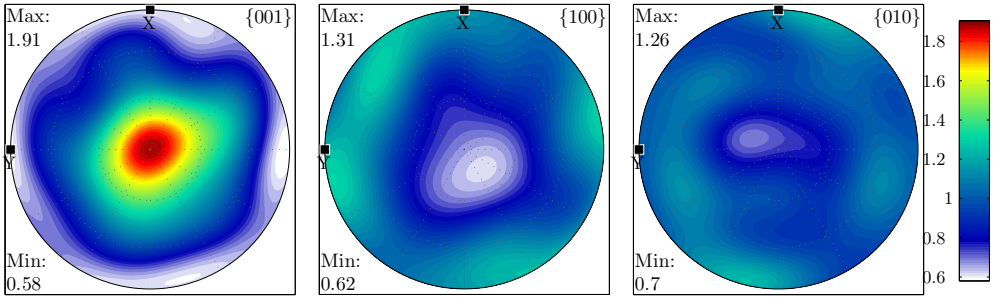

Figure 7: Pole figures from a discrete sampling ($N = 4800$) of Eq. 39 using the STAT method developed by Toth and van Houtte (1992).

the $SO(3)$ grid of orientation space is assigned a label, k, and the probability density integrated over the zone as

$$f_k = \int_k P(g)dg \tag{48}$$

where g represents an orientation and $P(g)$ is the probability density of that orientation. The discrete cumulative distribution is constructed by

$$F(j) = \sum_{k=1}^{j} f_k \tag{49}$$

such that $F(N_g) = 1$ where N_g is the total number of discrete orientations in the grid. A set of N integers, s, are randomly selected from a uniform distribution between 0 and 1. The discrete representation of the ODF is constructed by selecting the k^{th} orientations of the grid according to $k = H(s)$, where $x = H(y)$ is the inverse of the discrete cumulative distribution, $y = F(x)$.

The pole figures in Fig. 7 were generated from discrete ODFs constructed using the Toth and van Houtte (1992) algorithm with a $5^\circ \times 5^\circ \times 5^\circ$ grid of $SO(3)$ and $N = 4800$ discrete samples. The underlying analytical ODF is based on Eq. 39 for $\frac{d}{d_0} = 0.72$. The peak intensity is closer to the analytical value of 1.93 than the pole figure of Fig. 6. This is because the uniform grid generated by the HEALPix algorithm does not provide an initial orientation at precisely $\theta = 0$, whereas the Toth and van Houtte (1992) algorithm can favorably select orientations near $\theta = 0$ depending upon the grid used. However, the simulation-based approach results in more a uniform distribution that is generally in agreement with the underlying March solution than the Toth and van Houtte (1992) approach for these textures. A third alternative would be to use the grid generated by the HEALPix algorithm and adjust the volume fractions in accordance with the relative likelihood of each orientation as expressed by Eq. 39. We have not pursued that approach and consider the deformation simulation-based strategy sufficient.

4 Simulation Results

Using the elastic coefficients reported by Bedrov et al. (2009) and listed in Table 3, the thermal strains fit to lattice parameter measurements of Kolb and Rizzo (1979), and discrete orientation distributions based on the March model of texture evolution within the self-consistent homogenization scheme presented in Section 3, simulations were conducted to isolate the effects of porosity, crystal aspect ratio, and texture on thermal strain.

Comparison of homogenization approaches

A small subset of our simulations were conducted assuming zero porosity and a crystal aspect ratio of unity (spherical crystals) in order to compare the thermal expansion coefficients estimated using each of the homogenization schemes discussed in Section 3. Orientation distributions reflecting the isostatic case and unaxially die-pressed case were employed using the approach outlined above and assuming $\frac{d}{d_0} = 1.0$ and $\frac{d}{d_0} = 0.5$, respectively.

Linearized tangent coefficients of thermal expansion at $T = 23^\circ C$ in the axial and radial specimen directions are reported in Table 4 for three different population sizes, N, of the discrete orientation distribution.

Results for the isostatic case are not perfectly isotropic because of the discrete nature of the orientation distributions and low crystal symmetry. In particular, in the coordinate system employed here, the HEALPix algorithm does not align a [001] pole precisely along the specimen 'Z' axis and accordingly the axial CTEs are lower than radial. Clearly, as the number of discrete crystal orientations is increased the axial and radial CTEs are converging toward each other for all methods. In this case, the Reuss and Voigt bounds differ by a factor of two in thermal expansion, while the Hill average is within 6% of the self-consistent coefficient of thermal expansion.

For the textured case, the axial CTE estimated by the Reuss and Voigt schemes do not bound that computed using the self-consistent approach. The Voigt and Reuss averages provide upper and lower bounds on the strain energy of the composite, not on a term by term basis of any specific property. In this case, the self-consistent axial CTE is near the value estimated by the Reuss approximation, while the radial CTE is within 10% of that estimated using a Hill average.

With the exception of the self-consistent scheme, the homogenizations schemes compared in Table 4 do not account for non-spherical crystal geometry and, accordingly, these results are not reflective of any actual TATB-based composite. Instead, the results presented in Table 4 are included to offer a comparison between these approaches and demonstrate relative level of convergence in thermal expansion for the orders of discretization used here.

Comparison with experimental results

Rizzo et al. (1981) measured thermal expansion during temperature cycling of various TATB-based composites including explosives such as LX-17 and PBX-9502, and pure TATB "compacts" having no additional binder. They report values over the temperature ranges $T = -50°C$ to $-10^{-}°C$ and $T = 40°C$ to $70^{-}°C$ estimated as the slope of thermal strain with respect to temperature at the midpoint of these respective temperature ranges. The values measured by Rizzo et al. (1981) and the corresponding values computed using the self-consistent theory are compared in Table 5. Generally, the self-consistent theory appears to overpredict thermal expansion for the "isostatically pressed" case when compared to values measured by Rizzo et al. (1981). The extent of preferred orientation for the uniaxially die-pressed case is not reported; assuming a uniaxial consolidation and associated orientation distribution consistent with Eq. 39 and $\frac{d}{d_0} = 0.5$ the predicted axial coefficient of thermal expansion over the temperature range $T = 40°C$ to $70^{-}°C$ is slightly lower than the measured value. On the other hand the self-consistent estimate is larger than measured at the lower temperature range. It is difficult to pin down discrepancies in these results because the values of porosity, crystal aspect ratio, and extent of preferred orientation are not reported in Rizzo et al. (1981). Additionally, from details provided in Rizzo et al. (1981), the details of their computation of coefficient of thermal expansion from experimental data are not clear. It is plausible the calculation of such a derivative is sensitive to experimental "noise". We use these results as an indication of general agreement in overall trends, but note the quantitative discrepancy.

Cunningham et al. (2003) measured thermal expansion in axial and radial directions in repeated experiments using die-pressed pure TATB cylindrical specimens whose average density indicates a porosity of approximately 4%. Simulations of this experiment were performed assuming an orientation distribution consistent with Eq. 39, $\frac{d}{d_0} = 0.5$, and an average crystal aspect ratio of 1/200 (cf. Schwarz et al., 2013). The values of thermal strain measured in the axial and radial directions (Cunningham et al., 2003) are plotted as

Table 4: Predicted coefficients of thermal expansion for isotropic and textured polycrystal TATB predicted at $T = 23°C$ using various homogenization schemes. These comparisons reflect simulations of zero porosity and a crystal aspect ratio of unity (equiaxed crystals).

		Isostatic $\frac{d}{d_0} = 1$		Uniaxial $\frac{d}{d_0} = 0.5$	
Method	N	axial	radial	axial	radial
Reuss					
	4800	102.29	103.04	152.08	78.14
	9600	102.47	102.95	152.15	78.10
	16000	102.57	102.90	152.19	78.08
Voigt					
	4800	51.80	52.45	105.48	31.93
	9600	51.96	52.37	105.52	31.92
	16000	52.05	52.33	105.54	31.92
Hill					
	4800	77.05	77.75	128.78	55.03
	9600	77.21	77.66	128.83	55.01
	16000	77.31	77.61	128.87	55.00
Self-Consistent					
	4800	81.42	82.41	153.93	50.11
	9600	81.66	82.29	153.98	50.09
	16000	81.78	82.22	154.02	50.08

Table 5: Comparison of axial linearized coefficients of thermal expansion computed in this work with those measured by Rizzo et al. (1981) under similar conditions.

Method	Pressing	$T = -30°$C	$T = 55°$C
Experiment (Rizzo et al., 1981)	isostatic	40	76
Self-Consistent	$\frac{d}{d_0} = 1.0$	56	82
Experiment (Rizzo et al., 1981)	uniaxial die	69	129
Self-Consistent	$\frac{d}{d_0} = 0.5$	81	122

circles and diamonds, respectively, against temperature in Figure 8a. The solid and dashed lines represent results from self-consistent simulations for axial and radial specimen directions, respectively, corresponding to the discrete orientation distribution illustrated by the [001] pole figure in Fig. 8b. The agreement between measured and simulated thermal strains are good across this range in temperature, especially considering that the underlying single crystal lattice thermal expansion data was experimentally measured (and subsequently fit) only over the range $T = -57$ to $100°C$.

Similar data is presented by Souers et al. (2011) for "ultrafine" TATB composites that utilize TATB crystals that have been pulverized to a smaller characteristic diameter prior to consolidation. We performed a corresponding self-consistent simulation assuming 7% porosity and an aspect ratio of 1/27 (these parameters characteristic of the density and particle size distribution reported by Souers et al. (2011)) and the same orientation distribution illustrated in Fig. 8b. A comparison of these simulation results with the measurements reported in Souers et al. (2011) are shown in Fig. 9. In this case, the thermal strains at temperatures above ambient $T = 21°C$ are in good agreement. The simulated thermal strains at colder temperatures also match experimental values reasonably well.

Influence of porosity and crystal aspect ratio

Linearized coefficients of thermal expansion at $T = 55°C$ from simulations of various values of porosity are shown in Fig. 10. The black diamonds are from simulations using an aspect ratio that is representative of crystal morphology in "ultrafine" TATB specimens, while the green circles reflect results using an aspect ratio representing normal TATB crystal morphology. Porosity has a significant and similar effect of decreasing thermal expansion across the range 0 to 12% for both crystal aspect ratios.

The influence of crystal aspect ratio is demonstrated in Fig. 11 where linearized coefficients of thermal expansion at $T = 55°C$ are plotted versus the inverse of aspect ratio (crystal diameter divided by thickness). Fig. 11a includes results over a range of aspect ratios representative of "ultrafine" TATB speciments, while the aspect ratios in Fig. 11b are representative of normal TATB. Clearly, the influence of aspect ratio is more significant for crystals that are more nearly equiaxed. As the nominal crystal diameter grows (assuming a relatively fixed thickness), thermal expansion decreases. The drop-off in CTE appears to saturate or diminish with increasing diameter-to-thickness ratio.

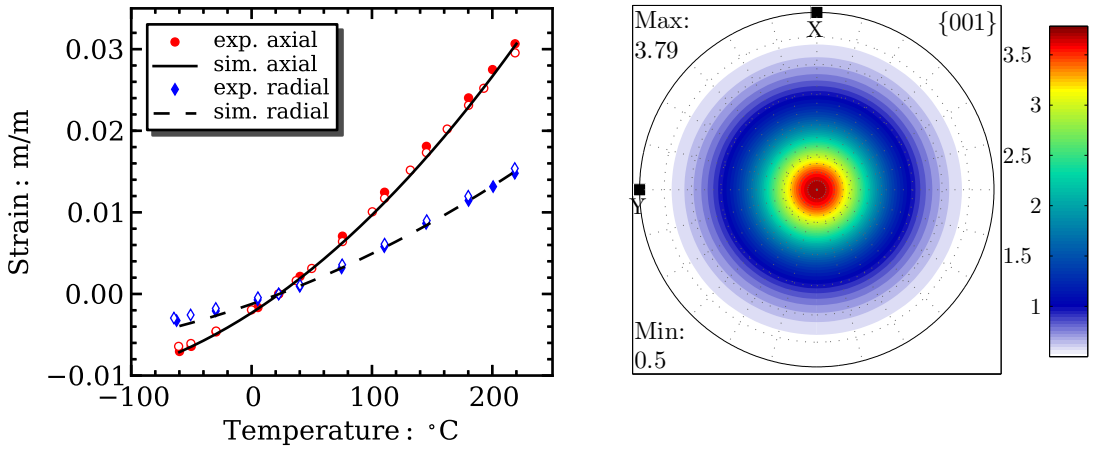

(a) Thermal Expansion

(b) 001 Pole Figure

Figure 8: Comparison of simulation results and experimental data for the anisotropic thermal expansion of unaxially (die) pressed specimens. The simulation results presented in (a) employed a distribution of crystal orientations illustrated by the [001] pole figure shown in (b). The orientation distribution corresponds to a uniaxial consolidation of $\frac{d}{d_0} = 0.5$. The simulation employed a distribution of crystals whose aspect ratio was 1/200 and a porosity of 0.04 (equivalent to 96% TMD.)

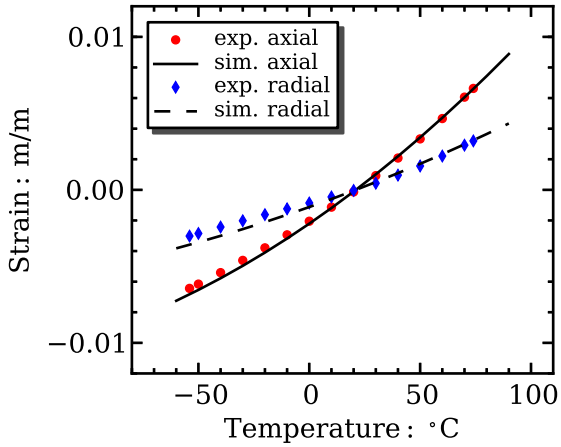

Figure 9: Comparison of simulation results and experimental data for the anisotropic thermal expansion of unaxially (die) pressed specimens. The simulation employed the same distribution of crystal orientations illustrated by the [001] pole figure shown in Fig. 8b corresponding to a uniaxial consolidation of $\frac{d}{d_0} = 0.5$. The simulation employed a distribution of crystals whose aspect ratio was 1/27 and a porosity of 0.07 (equivalent to 93% TMD.)

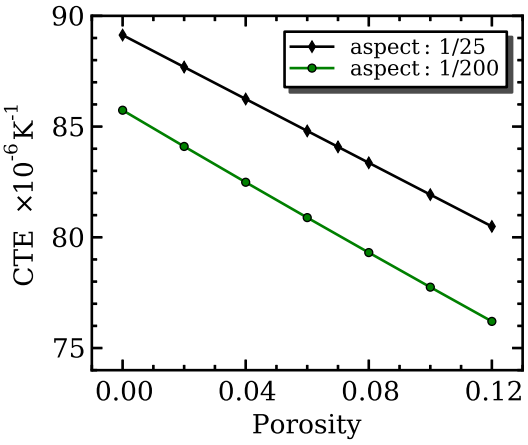

Figure 10: Plot illustrating the influence of porosity on the computed tangent coefficient of thermal expansion of isotropic (non-textured) polycrystal TATB at $T = 55°C$.

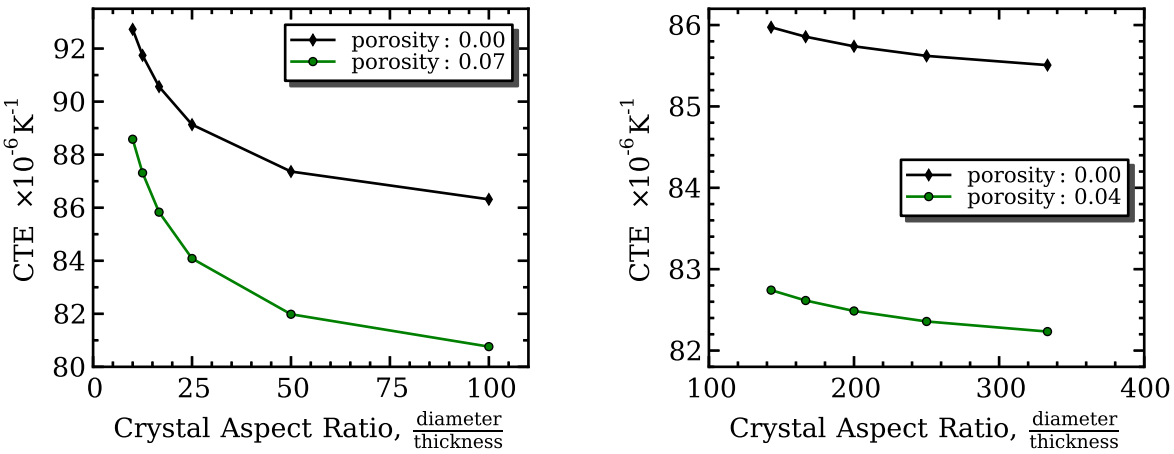

(a) ultra-fine TATB

(b) normal TATB

Figure 11: Plots illustrating the influence of crystal aspect ratio (diameter / thickness) on the computed tangent coefficient of thermal expansion of isotropic (non-textured) polycrystal TATB at $T = 55°C$. The range of aspect ratios included in (a) are representative of "ultra-fine" particle size distribution and that of (b) represents normal TATB aspect ratios.

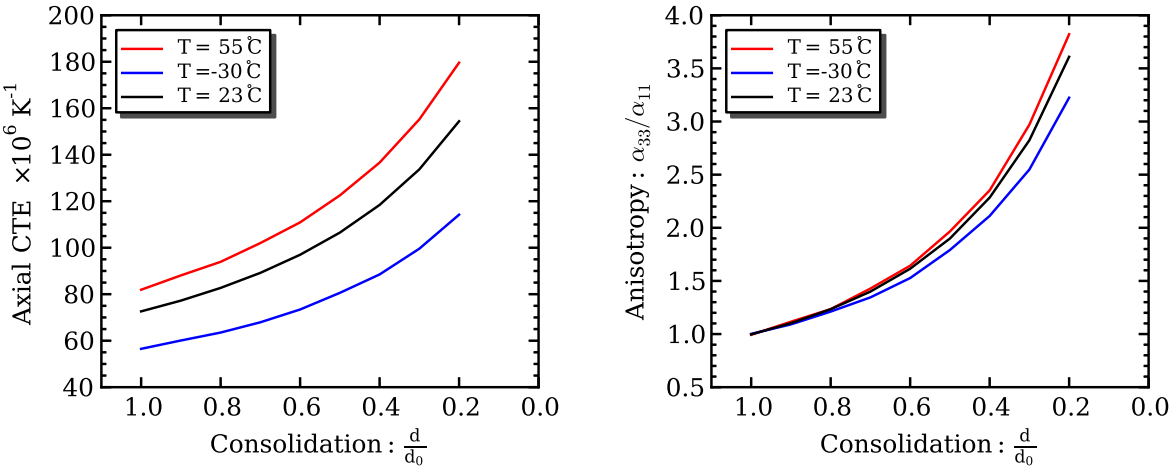

(a) (b)

Figure 12: Effects of texture induced from uniaxial die-pressing of cylindrical specimens. (a) Plot of axial tangent CTE versus the ratio of compressed to initial thickness (principal stretch), $\frac{d}{d_0}$. (b) Plot of anisotropy in tangent CTEs, $\frac{\alpha_{33}}{\alpha_{11}}$, versus consolidation $\frac{d}{d_0}$

Influence of texture

It is clear from experimental findings (Cady, 1975; Rizzo et al., 1981; Cunningham et al., 2003; Souers et al., 2011) that the preferred orientation of TATB crystal [001] poles attributed to uniaxial die pressing leads to anisotropy (an axisymmetric transverse isotropy) in thermal expansion. Simulation results presented in Figs. 8 and 9 represent the first model connecting the evolution of orientation distribution during uniaxial pressing to predicted anisotropic thermal strains. Similar simulations were conducted over a range of consolidation parameter values, i.e. $\frac{d}{d_0}$, to study the influence of consolidation on thermal expansion. Fig. 12a illustrates the relationship between linearized coefficients of thermal expansion at three temperatures over a range of the texture strength. Clearly, texture has a more pronounced influence on thermal expansion than porosity or aspect ratio, especially considering that most experimental data has been collected by measuring only the axial component of deformation. Fig. 12b plots the observed anisotropy versus texture strength. Combined, these results highlight that, for components manufactured via a consolidation process characterized by spatially variable deformation (e.g. cf. Schwarz et al., 2013) field, the magnitudes of thermal expansion and associated anisotropy will exhibit spatial variation throughout the component.

5 Discussion

The simulation results presented above quantify the influence of microstructure on thermal expansion of polycrystal TATB. The trends identified in this modeling are expected to be applicable to TATB-based explosives such as PBX-9502 and LX-17. For example, the influence of aspect ratio on thermal expansion is not that important to the qualitative understanding of the response of engineered components, in part because it is a smaller effect numerically, and, perhaps more importantly, because the particle size distributions are relatively uniform spatially and do not change temporally. Quantitatively, aspect ratio must be included in

continuum homogenization models, but variability of aspect ratios about a nominal value is not likely to make a large contribution to overall material variability.

On the other hand, increasing porosity is clearly associated with a marked decrease in rates of thermal expansion. While a focused experimental investigation to confirm this relationship has not been conducted, existing experimental data points are consistent with the observation. During repeated temperature cycles of TATB-based composites, the volume of a specimen will exhibit an accumulating permanent volumetric growth. This behavior, referred to as "thermal ratchet growth", is not specifically included in the present model, but we can make a phenomenological connection. Asserting that mass is conserved within the material, volumetric parts of thermal ratchet growth are accommodated by a decrease in material density, or equivalently, an increase in porosity. Thus, according to our model, reduced rates of thermal expansion for ratcheted specimens are expected and are indeed observed in experiment (e.g. Rizzo et al., 1981).

Likewise, the development of preferred orientation of TATB [001] poles has a distinct influence on the magnitude and orientation of thermal expansion for a polycrystal component. The model presented here has been applied to exploring the relationship between axial and radial thermal expansion behavior in uniaxial or die-pressed specimens. The same model can be applied to understanding the development of texture and associated anisotropic thermal expansion for engineered components of arbitrary geometry if sufficient information about the pressing operation is known to estimate the spatial deformation field, i.e. $\mathbf{F}(\mathbf{x})$. A critically important point established in this work is that the anisotropy depends not only on the actual 'preferred orientation', but also on the magnitude of deformation or, equivalently, extent of preferential alignment along the orientation as well. It is anticipated (cf. results of Schwarz et al., 2013) that the pressing of engineered components results in significant spatial variation of deformation in both magnitude and orientation. Consequently, there likely exists a spatial variation in the anisotropy and orientation of thermal expansion behavior within a manufactured part. Even under macroscopically unconstrained thermal expansion, non-zero macroscale stresses can arise when the thermal expansion tensor is nonuniform. Furthermore, for constrained thermal expansion, the distribution of stresses are likely to be nonuniform as well. Such behavior may prove to be important, for example, in predicting the long term creep and relaxation of explosive components under storage conditions.

It is feasible to apply the modeling approach presented here to predicting the spatially nonuniform thermal expansion of engineered components within larger assembled systems. To do so, an estimate of the spatial deformation field from the pressing or consolidation process is required. Then, using the spatial distribution $\mathbf{F}(\mathbf{x})$ and the algorithm of Eqs. 41-47, one can obtain a spatially varying orientation distribution $\mathcal{O}(\mathbf{F}(\mathbf{x}))$. Finally, solving Eqs. 23 and 24 will lead to a self-consistent estimate of spatially varying, nonlinear thermal expansion.

6 Conclusions

In this work we have, for the first time, developed a mesoscale continuum model relating the thermal expansion of polycrystal TATB specimens to their microstructural characteristics. Specifically, our model includes a representation of grain aspect ratio, porosity, and crystallographic texture attributed to the consolidation process. An algorithm was built upon the March (1932) theory for particle alignment during consolidation in order to develop discrete orientation distributions consistent with arbitrary deformation

histories. Analytical and numerical solutions using this model were shown to produce textures consistent with previous measurements and characterization for isostatic and uniaxial die-pressed specimens. Predicted thermal strain versus temperature for textured specimens were shown to be in agreement with corresponding experimental measurements. Using the model, several simulations were run to investigate the influence of microstructure on macroscopic thermal expansion behavior. From these simulations we advance the following conclusions.

- Porosity and grain aspect ratio have an influence on the thermal expansion of polycrystal TATB over reasonable ranges.
- Preferred orientation of [001] poles in single crystal TATB within a polycrystal give rise to pronounced anisotropy of the macroscopic thermal expansion.
- The extent of this preferred orientation depends on the magnitude of deformation, and consequently, is expected to vary spatially throughout manufactured components much like porosity.
- The modeling approach developed here has utility toward bringing spatially variable microstructural features into macroscale system engineering models.

Presently, the developed self-consistent model lacks any accounting of polymeric binder. Given the similarity of thermal expansion coefficients for typical polymer binder and bulk polycrystal TATB, supporting experimental evidence, and the small volume fraction of binder in explosives, it is expected that the binder will have only a small influence on the overall thermal expansion. Future extensions of this work will address the effects of binder. In particular, binder cannot be treated in the same manner as the volume fractions of crystals and pores. The low volume fraction of binder is morphologically closer to a thin shell of binder surrounding the ellipsoidal crystal inclusions. Such morphology is beyond the direct application of the self-consistent theory employed here, although there have been various extensions to the theory to treat precisely this case (Smith, 1974; Christensen and Lo, 1979; Bornert, 1996).

Additionally, the scope of this work has been restricted to understanding the relationship between microstructure and thermal expansion behavior. This relationship is an important first step towards understanding and modeling the ratcheting observed in TATB-based composites during repeated temperature cycles. Ongoing work to extend the self-consistent modeling scheme to account for relaxation of internal strain energy by asymmetric intergranular slip will enable future mesoscale modeling of thermal ratchet growth.

Acknowledgements

The author is grateful for the ongoing technical collaboration with Miles Buechler and Nathan Miller (W-13) which has provided a helpful sounding board in developing these ideas. The time spent by Ricardo Schwarz (MST-8) in explaining details of his preferred orientation model, texture measurements, and the resulting discussions are appreciated. The author is thankful for discussions with Ricardo Lebensohn (MST-8) on details of the numerical calculation of Eshelby's tensor and John Carpenter (MST-6) on details of pole figure analysis software. Additionally, the detailed reviews and feedback of this manuscript from Matt Lewis,

Devin Shunk, and Bob Stevens (W-13) have improved communication of key points. The author is also thankful for correspondence with Bruce Cunningham (LLNL) to clarify details of the experiments used for comparisons with this work and Cary Skidmore (W-6) for tracking down internal correspondence containing the orientation distributions measured by Cady.

References

Baker, D. W., Chawla, K. S., Krizek, R. J., Sep. 1993. Compaction fabrics of pelites - experimental consolidation of kaolinite and implications for analysis of strain in slate. Journal of Structural Geology 15 (9-10), 1123–1137.

Bauchau, O. A., Trainelli, L., Apr. 2003. The vectorial parameterization of rotation. Nonlinear Dynamics 32 (1), 71–92.

Bedrov, D., Borodin, O., Smith, G. D., Sewell, T. D., Dattelbaum, D. M., Stevens, L. L., Dec. 2009. A molecular dynamics simulation study of crystalline 1,3,5-triamino-2,4,6-trinitrobenzene as a function of pressure and temperature. Journal of Chemical Physics 131 (22), 224703.

Bornert, M., Feb. 1996. A generalized pattern-based self-consistent scheme. Computational Materials Science 5 (1-3), 17–31.

Cady, H., April 1975. WX-2 Monthly Report. Tech. Rep. WX-2-MR-75-4, Los Alamos Scientific Laboratory.

Cady, H. H., Larson, A. C., 1965. Crystal structure of 1,3,5-triamino-2,4,6-trinitrobenzene. Acta Crystallographica 18, 485–&.

Christensen, R. M., Lo, K. H., 1979. Solutions for effective shear properties in 3 phase sphere and cylinder models. Journal of the Mechanics and Physics of Solids 27 (4), 315–330.

Cunningham, Tran, Weese, Lewis, Harwood, Healy, 2003. Coefficients of thermal expansion and ratchet growth measurements on tatb based plastic bonded explosives and constituents. Tech. rep., Lawrence Livermore National Laboratory.

Dollase, W. A., Jan. 1986. Correction of intensities for preferred orientation in power diffractometry: application of the march model. Journal of Applied Crystallography 19, 267–72.

Eshelby, J. D., 1957. The determination of the elastic field of an ellipsoidal inclusion, and related problems. Proceedings of the Royal Society of London Series A-mathematical and Physical Sciences 241 (1226), 376–396.

Gee, R., Roszak, S., Balasubramanian, K., Fried, L., 2004. Ab initio based force field and molecular dynamics simulations of crystalline tatb. Journal of Chemical Physics 120, 7059–7066.

Gee, R. H., Maiti, A., Fried, L. E., Jun. 2007. Mesoscale modeling of irreversible volume growth in powders of anisotropic crystals. Applied Physics Letters 90 (25), 254105.

Gorski, K. M., Hivon, E., Banday, A. J., Wandelt, B. D., Hansen, F. K., Reinecke, M., Bartelmann, M., Apr. 2005. HEALPix: A framework for high-resolution discretization and fast analysis of data distributed on the sphere. Astrophysical Journal 622 (2), 759–771.

He, Y. L., Jonas, J. J., 2009. Rodrigues-Frank spaces for misorientations and orientation relationships between crystals of any two crystallographic point groups. Applications of Texture Analysis 201, 269–280.

Hill, R., 1965. Continuum micro-mechanics of elastoplastic polycrystals. Journal of the Mechanics and Physics of Solids 13 (2), 89–101.

Kocks, U., Tome, C., Wenk, H., 1998. Texture and Anisotropy: Preferred Orientations in Polycrystals and their Effect on Materials Properties. Cambridge University Press.

Kolb, J., Rizzo, H., 1979. Growth of 1,3,5-triamino-2,4,6-trinitrobenzene (TATB) .1. anisotropic thermal-expansion. Propellants and Explosives 4 (1), 10–16.

Lebensohn, R. A., Tome, C. N., Castaneda, P. P., 2007. Self-consistent modelling of the mechanical behaviour of viscoplastic polycrystals incorporating intragranular field fluctuations. Philosophical Magazine 87 (28), 4287–4322.

Lebensohn, R. A., Tome, C. N., Maudlin, P. J., Feb. 2004. A self-consistent formulation for the prediction of the anisotropic behavior of viscoplastic polycrystals with voids. Journal of the Mechanics and Physics of Solids 52 (2), 249–278.

Maienschein, J. L., Garcia, F., Feb. 2002. Thermal expansion of TATB-based explosives from 300 to 566 k. Thermochimica Acta 384 (1-2), 71–83.

Maiti, A., Gee, R. H., Hoffman, D. M., Fried, L. E., Mar. 2008. Irreversible volume growth in polymer-bonded powder systems: Effects of crystalline anisotropy, particle size distribution, and binder strength. Journal of Applied Physics 103 (5), 053504.

March, A., Feb. 1932. Mathematical theory on regulation according to the particle shape and affine deformation. Zeitschrift Fur Kristallographie 81 (3/4), 285–297.

Owens, W. H., 1973. Strain modification of angular density distributions. Tectonophysics 16 (3-4), 249–261.

Rai, N., Bhatt, D., Siepmann, J. I., Fried, L., 2008. Monte carlo simulations of 1,3,5,-triamino-2,4,6-trinitrobenzene (TATB): Pressure and temperature effects for the solid phase and vapor-liquid phase equilibria. The Journal of Chemical Physics 129, 194510.

Rizzo, H. F., Humphrey, J. R., Kolb, J. R., 1981. Growth of 1,3,5-triamino-2,4,6,-trinitrobenzene (TATB) .2. control of growth by use of high-tg polymeric binders. Propellants and Explosives 6 (3), 57–62.

Schlenker, J. L., Gibbs, G. V., Boisen, M. B., 1978. Strain-tensor components expressed in terms of lattice-parameters. Acta Crystallographica Section A 34 (JAN), 52–54.

Schwarz, R. B., Brown, G. W., Thompson, D. G., Olinger, B. W., Furmanski, J., Cady, H. H., 2013. The effect of shear strain on texture in pressed plastic bonded explosives. Propellants, Explosives, Pyrotechnics 38, 685–694.

Sewell, T. D., 1996. Monte carlo simulations of crystalline TATB. Materials Research Society Symposium Proceedings 418, 67–72.

Skidmore, C. B., Butler, T. A., Sandoval, C. W., January 2003. The elusive coefficients of thermal expansion in PBX 9502. Tech. Rep. LA-14003, Los Alamos National Laboratory.

Smith, J. C., 1974. Correction and extension of Vanderpoels method for calculating shear modulus of a particulate composite. Journal of Research of the National Bureau of Standards Section A-physics and Chemistry A 78 (3), 355–361.

Souers, P. C., Lewis, P., Hoffman, M., Cunningham, B., Aug. 2011. Thermal expansion of LX-17, PBX 9502, and ultrafine TATB. Propellants Explosives Pyrotechnics 36 (4), 335–340.

Suh, I.-H., Park, Y.-S., Kim, J.-G., 2000. ORTHON: Transformation from triclinic axes and atomic coordinates to orthonormal ones. Journal of Applied Crystallography 33, 994.

Sun, J., Kang, B., Xue, C., Liu, Y., Xia, Y., Liu, X., Zhang, W., 2010. Crystal state of 1,3,5-triamino-2,4,6-trinitrobenzene (TATB) undergoing thermal cycling process. Journal of Energetic Materials 28, 189–201.

Taylor, D., 2013. Intermolecular forces and molecular dynamics simulation of 1,3,5-triamino-2,4,6-trinitrobenzene (TATB) using symmetry adapted perturbation theory. The Journal of Physical Chemistry 117, 3507–3520.

Toth, L. S., van Houtte, P., 1992. Discretization techniques for orientation distribution functions. Textures and Microstructures 19 (4), 229–244.

Valenzano, L., Slough, W. J., Perger, W. F., 2012. Accurate prediction of second-order elastic constants from first principles: PETN and TATB. Shock Compression of Condensed Matter - 2011, Pts 1 and 2, Amer Phys Soc (APS) 1426, 1191–1194.

Walpole, L. J., 1969. On overall elastic moduli of composite materials. Journal of the Mechanics and Physics of Solids 17 (4), 235–251.

Zhang, H., Sun, J., Kang, B., Shu, Y., Shu, X., Liu, Y., Liu, X., 2012. Crystal morphology controlling of tatb by high temperature anti-solvent recrystallization. Propellants, Explosives, and Pyrotechnics 37, 172–178.

Zolotoyabko, E., Dec. 2013. Fast quantitative analysis of strong uniaxial texture using a March-Dollase approach. Journal of Applied Crystallography 46, 1877–1879.